Influence of substrate on interfacial Dzyaloshinskii-Moriya interaction in epitaxial Tm$_3$Fe$_5$O$_{12}$ films

Takian Fakhrul [ORCID],[*] Siying Huang [ORCID],[*] Yixuan Song, Bharat Khurana, Geoffrey S. D. Beach,[†] and Caroline A. Ross [ORCID][‡]

Department of Materials Science and Engineering, Massachusetts Institute of Technology, Cambridge, Massachusetts 02139, USA

The interfacial Dzyaloshinskii-Moriya interaction (iDMI) promotes homochiral magnetic structures such as Néel-type domain walls (DWs) and skyrmions. iDMI as well as chiral magnetic structures have been demonstrated in metal/garnet heterostructures offering desirable properties for spintronic applications compared to their metallic counterparts. By measuring the motion of DWs as a function of current and in-plane magnetic field, we show that for 6.6 nm thick epitaxial thulium iron garnet films with perpendicular magnetic anisotropy grown on gallium garnet substrates, the iDMI and the DW width depend on the substrate but do not scale linearly with lattice mismatch strain. The largest iDMI was 0.007 mJ m^{-2}, obtained for three substrates of different compositions. The total anisotropy, however, does increase linearly with lattice parameter, indicating a dominant magnetoelastic anisotropy contribution. The sensitivity of iDMI and anisotropy to substrate composition provides opportunities for engineering homochiral magnetic structures and their dynamics.

I. INTRODUCTION

The Dzyaloshinskii-Moriya interaction (DMI) [1,2] is a key ingredient for the stabilization and current-driven manipulation of homochiral magnetic structures such as Néel-type skyrmions [3–8] and domain walls (DWs) [8–11], which have been proposed to represent bits in next-generation spintronic data storage and processing devices [12,13]. DMI requires broken inversion symmetry and can manifest in certain bulk materials that are intrinsically chiral [14–18], but it is more easily obtained and engineered in thin-film systems which break inversion symmetry at the interfaces [19]. There have been extensive studies of thin-film systems with interfacial DMI (iDMI), of which metallic magnets interfaced with heavy metals (HMs) have attracted the most attention [5–7,10,11]. The HM layer serves as a source of spin current [6,11] via the spin Hall effect (SHE) [20,21] and supplies the strong spin-orbit coupling that is necessary for the iDMI [3,22].

Ferrimagnetic iron garnets have attracted a great deal of attention in recent years for spintronic applications, simultaneously offering ultralow damping and the absence of charge currents and Joule heating compared to metallic systems [23–25]. Iron garnet films exhibit iDMI, and current-driven dynamics of homochiral skyrmions and DWs have been demonstrated in HM/garnet heterostructures [26–30]. While HM/garnet/substrates show desirable spintronic properties, their iDMI is not well understood compared to that of their metallic counterparts [3,22,31], and the origin of the iDMI remains a topic of active debate [32]. Some studies have attributed the iDMI to the garnet/substrate interface [33,34], while others claim it originates at the metal/garnet interface [35–37]. There have been several attempts to disentangle the contributions from the metal/garnet and the garnet/substrate interfaces [28,30,31,34,38]. In addition, although the reported chirality of magnetic textures produced by the metal/garnet interface is right handed (with metal on top) [28,31], both chiralities of the lower interface iDMI have been observed [28,30,31]. There are also ambiguities resulting from differences in sample preparation and probing techniques [37]. Recent studies have suggested a dependence of iDMI on the species of metal capping layer [31,36,38], the rare-earth spin-orbit coupling [31], and the strain induced by garnet-substrate lattice mismatch [31,38,39]. The observation of nonzero iDMI in garnet/substrate systems without a capping layer emphasizes the crucial role of the garnet/substrate interface in inducing the iDMI [28,34]. However, a direct comparison of the iDMI of garnet on various garnet substrates has not yet been presented.

Here by observing DW depinning behavior, we show that iDMI arises in a Pt/Tm$_3$Fe$_5$O$_{12}$ (TmIG) thin film on various garnet substrates, producing right-handed chirality. Pt is selected as a chemically stable layer that provides the spin current needed in the measurements and is grown at the same time on all of the samples. The magnitude of iDMI depends on the substrate but does not show a simple trend with lattice mismatch. Furthermore, the measurements show that the DW width can be engineered by tuning the magnetoelastic anisotropy, as expected from previous work [40–44]. These results open avenues to further investigation of the source and mechanisms for iDMI in garnet thin films and are relevant to the engineering of next-generation spintronic devices, especially racetracks where bits are encoded by DWs or skyrmions.

II. CHARACTERIZATION

TmIG films with a thickness of 6.6 nm were deposited using pulsed laser deposition (PLD) on five different single-crystal gallium garnet substrates as described in Sec. VI. All of the substrates are (111) oriented. We extract the out-of-plane (OP) lattice parameter of the films from

---

[*]These two authors contributed equally to this work.
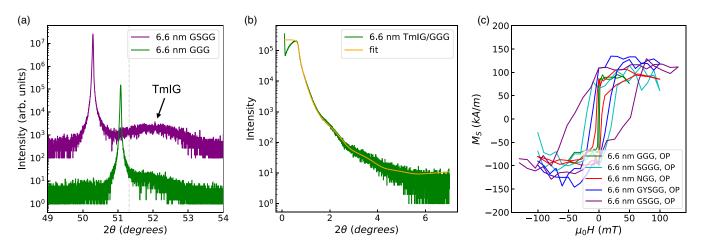
[†]gbeach@mit.edu

[‡]caross@mit.edu

FIG. 1. Magnetic and structural characterization of the garnet samples. (a) HRXRD ω-2θ scans of 6.6 nm TmIG films on GGG and GSGG around the (444) substrate peak. The nominal 2θ position of unstrained TmIG is marked by the gray dashed line. (b) Example HRXRR scan of the TmIG film on GGG. (c) OP magnetic hysteresis loops from VSM of 6.6 nm TmIG films on various substrates.

high-resolution x-ray diffraction (HRXRD) fitting [Fig. 1(a)], and we conclude that all the films are uniform in thickness from the fits to the Kiessig fringes in high-resolution x-ray reflectometry [HRXRR; Fig. 1(b)]. The symmetric HRXRD scans [Fig. 1(a)], as well as reciprocal space map (RSMs) of thicker films in our prior work [42,45] show that all films grew coherently with in-plane (IP) tensile strain due to lattice mismatch between TmIG (bulk cubic lattice parameter of 1.2324 nm [46]) and $Gd_3Ga_5O_{12}$ (GGG, 1.2376 nm), $Gd_{2.6}Ca_{0.4}Ga_{4.1}Mg_{0.25}Zr_{0.65}O_{12}$ (SGGG, 1.2480 nm), $Nd_3Ga_5O_{12}$ (NGG, 1.2505 nm), $Gd_{0.63}Y_{2.37}Sc_2Ga_3O_{12}$ (GYSGG, 1.2507 nm), and $Gd_3Sc_2Ga_3O_{12}$ (GSGG, 1.2554 nm) [47]. The bulk magnetostriction value λ_{111} of TmIG is -5.2×10^{-6}, favoring perpendicular magnetic anisotropy (PMA) for epitaxial films with sufficiently large IP tensile strain. Film uniformity was characterized in our previous scanning transmission electron microscopy (STEM) results such as Fig. 1(e) in Ref. [42] and Fig. 1(c) in Ref. [31]. We do not expect the films to form secondary phases because TmIG is itself a stable phase at equilibrium and its growth is further stabilized by epitaxy, making the emergence of other phases highly unlikely. This is also evidenced by measurements of thicker garnet films, which did not show secondary phases [31,42].

The magnetic properties of the films were characterized by vibrating sample magnetometry (VSM) measurements. The OP VSM hysteresis loops in Fig. 1(c) show the films have a perpendicular easy axis with near-bulk saturation magnetization M_s of 110 kA m^{-1}. The magnetization of the 6.6 nm films agrees with that measured for a similarly prepared series of film thicknesses described elsewhere [31] which indicated a dead layer thickness of 1.4 nm attributed to intermixing at the substrate interface. The large paramagnetic background signal of the substrates precluded background subtraction for the IP hysteresis loops of the TmIG films. The magnetic anisotropy of the TmIG films includes contributions from magnetocrystalline, magnetoelastic, and shape anisotropies. The net anisotropy constant $K_{u,\text{eff}}$ is defined as the difference between magnetic energy E for magnetization oriented IP vs OP. For epitaxial films lattice matched to a (111)-oriented substrate, $K_{u,\text{eff}}$ is given by

$$K_{u,\text{eff}} = E_{\text{OP}} - E_{\text{IP}} = -K_1/12$$
$$+ (9/4)\lambda_{111}c_{44}(\pi/2 - \beta) - \mu_0 M_s^2/2. \quad (1)$$

In this expression K_1 is the first-order cubic magnetocrystalline anisotropy constant, c_{44} is the shear modulus, β is the corner angle of the rhombohedrally distorted unit cell, and M_s is the saturation magnetization. K_1 is small ($\sim$100 J m^{-3}), and its contribution is negligible; therefore, when the magnetoelastic anisotropy overcomes the shape anisotropy, the films exhibit PMA.

III. PMA FROM SPIN HALL MAGNETORESISTANCE MEASUREMENTS

To investigate the substrate dependence of PMA, we performed spin Hall magnetoresistance (SMR) measurements on the TmIG sample series. The bilayers were patterned into Hall cross devices as shown schematically in Fig. 2(a). When an IP electrical current is applied in the Pt layer, the SHE in Pt induces a spin current in the z direction. When incident on the Pt/TmIG interface the spin current will partially reflect with a magnitude that depends on the relative orientation between the spin current polarization direction and the TmIG magnetization direction. The backflow of the spin current will, in turn, modulate the charge current in the Pt layer by the inverse SHE [48] and thus the measured longitudinal and transverse resistance. The transverse Hall resistance R_H in our experiment can be expressed as [45,49–51]

$$R_H = R_H^{\text{SMR}}\sin^2\theta\sin 2\psi + R_H^{\text{AHE,SMR}}\cos\theta + R_H^{\text{OHE}}H_z, \quad (2)$$

where θ and ψ describe the orientation of magnetization **m** in the TmIG layer as defined in Fig. 2(a). R_H^{SMR} and $R_H^{\text{AHE,SMR}}$ represent the manifestation of SMR and the SMR-induced anomalous Hall effect (AHE) resistance, and the R_H^{OHE} term
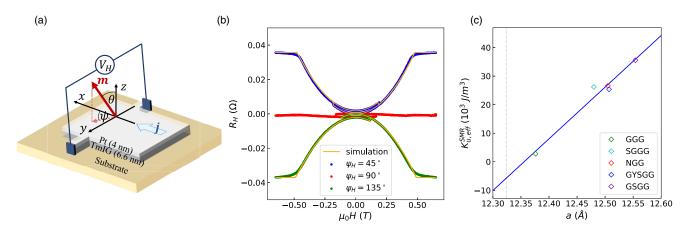
FIG. 2. Substrate dependence of PMA in TmIG. (a) Hall device schematics of the SMR measurements on the Pt/TmIG samples, including the coordinate system and the electrical setup. (b) Exemplary Hall resistance R_H of a Hall device on Pt/TmIG/NGG, measured as a function of applied IP field H along the directions $\psi_H = 45°$, $90°$, and $135°$. The anisotropy $K_{u,\text{eff}}$ is extracted from the saturation field $H_{K,\text{eff}}$ of the $45°$ and $135°$ curves. The orange solid curves are simulations reproducing the experimental data, which gives $\mu_0 H_{K,\text{eff}} = 0.4834$ T. The switching events of R_H around 0.2 T correspond to the magnetization switching caused by the small unintentional OP component of the IP field, manifesting as an AHE component [Eq. (2)]. (c) $K_{u,\text{eff}}$ as a function of lattice parameter a. The gray dashed line corresponds to the lattice parameter of bulk TmIG.

corresponds to the ordinary Hall effect. In our measurements, an IP field H is applied along angle ψ_H to reorient **m** in a plane that contains the z axis and forms an angle ψ_H with the x axis. In other words, we have $\psi = \psi_H$ given that the IP anisotropy is negligible in our system. As H increases, **m** rotates towards the IP direction, and R_H changes accordingly, until **m** is pulled fully IP and R_H saturates [Fig. 2(b)]. This saturation threshold $H_{K,\text{eff}}$, the anisotropy field, is given by $H_{K,\text{eff}} = \frac{2K_{u,\text{eff}}}{\mu_0 M_s}$, where $K_{u,\text{eff}} \equiv K_u - \frac{\mu_0}{2} M_s^2$ [Eq.(1)] is the effective uniaxial anisotropy, which differs from the magnetoelastic + magnetocrystalline anisotropy K_u by the magnetostatic energy term $\frac{\mu_0}{2} M_s^2$. From Eq. (2) we can see that when $\psi_H = 45°$ or $135°$, the Hall signal has the largest field-dependent variation, while **m** is reoriented by H and θ spans over the $[0, 90°]$ range. When $\psi_H = 0°$ or $90°$, the variation is minimized.

All electrical measurements were performed using a standard lock-in technique (see Sec. VI). We measured R_H as a function of H under the conditions of $\psi_H = 45°$, $135°$, or $90°$ [Fig. 2(b)]. By fitting the result to a macrospin simulation, we obtain, for example, $\mu_0 H_{K,\text{eff}} = 0.4834$ T and extract $K_{u,\text{eff}} = 27.80 \times 10^3$ J/m³ for Pt/TmIG/NGG. Figure 2(c) shows the extracted $K_{u,\text{eff}}$ values as a function of substrate lattice parameter a. As expected, the data points show a linear trend, corresponding to the scenario of strain-induced PMA. The intercept with the TmIG lattice parameter (gray dashed line) is -6.0 ± 3.4 kJ/m³, which is in reasonable agreement with the expected magnetostatic energy term $\frac{\mu_0}{2} M_s^2 = 7.60$ kJ/m³. Using the expression $K_u \equiv \frac{9}{4}\lambda_{111} c_{44}(\frac{\pi}{2} - \beta)$ [40–44] and the geometry of the rhombohedrally distorted unit cell, whose IP dimensions are matched to those of the substrate, we extract the magnetostriction $\lambda_{111} = (-1.1 \pm 0.1) \times 10^{-6}$ from the slope of K_u vs β. The smaller than bulk value may indicate a nonideal rare earth (RE):Fe stoichiometry. c_{44} is taken to be that of yttrium iron garnet (YIG), 766 GPa [46], justified by the fact that the shear modulus of RE garnets has only a small dependence (~0.5%) on the RE ion [52].

IV. DOMAIN WALL WIDTH AND iDMI FROM SPIN HALL TORQUE MAGNETOMETRY

The spin Hall torque magnetometry technique [53] allows us to probe the DW orientation as a function of external IP field H_x, from which we can extract the iDMI strength D and DW width Δ (see Sec. VI). The Pt/TmIG bilayers were patterned into DW tracks [Fig. 3(a)], and a dc current j was injected along the track in the Pt layer. A spin current due to the SHE of Pt is pumped into the magnetic TmIG layer, inducing spin-orbit torque (SOT) to act on the local magnetization [20,21] in the DW, which helps or hinders the domain depinning process from a local pinning site. The effect can be described by an OP effective field $H_{\text{eff}} \equiv \chi j$ acting on the DW. χ, the spin Hall efficiency, reveals the DW orientation by $\chi \equiv \chi_0 \cos\psi$ (see Sec. VI).

The experiment was performed by observing DW depinning events as a function of current and applied magnetic field. Exemplary results for TmIG/NGG are summarized in Fig. 3. Figure 3(a) shows a depinning event observed by wide-field magneto-optic Kerr effect (MOKE) (see Sec. VI) on a 10 µm wide DW track. During the measurement, a DW was first nucleated by SOT switching, moved by an OP field pulse, and pinned at a pinning site on the center of the track [Fig. 3(a)]. DW depinning and propagation events are driven by an OP field H_z with the assistance of current j, manifesting as the effective field $H_{\text{eff}} \equiv \chi j$. In the absence of the current and IP field, a typical OP field required for a wall to depin is ~55 Oe. The change in the depinning field with and without current δH_{dp} corresponds to H_{eff}. Its slope versus j yields $\chi \equiv \chi_0 \cos\psi$ [Fig. 3(b); see Sec. VI], where ψ is the magnetization orientation within the DW. The nonzero slope with $H_x = 0$ indicates a Néel character of the DW under equilibrium, thus nonzero iDMI. Under the application of various H_x the wall can change orientation to Bloch ($\mu_0 H_x = -4$ mT) or Néel ($\mu_o H_x = 24$ mT) or even reverse chirality [$\mu_0 H_x = -24$ mT; Fig. 3(c)].
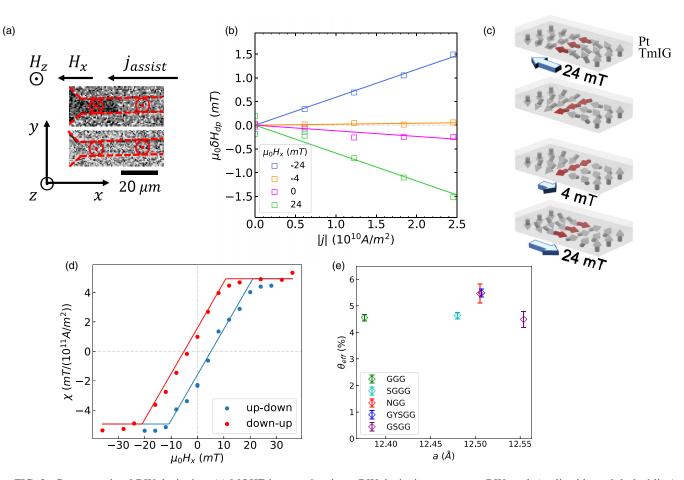
FIG. 3. Current-assisted DW depinning. (a) MOKE images showing a DW depinning event on a DW track (outlined by red dashed line) patterned on Pt/TmIG/NGG, together with the positive directions of the applied current and field. The down-up wall is pinned by a pinning site in the top frame and depinned and propagated to the left in the bottom frame. (b) Change in the depinning field δH_{dp} for down-up DWs as a function of dc current density $|j|$ for exemplary IP fields H_x. We obtain δH_{dp} for a certain $|j|$ from $(H_{dp,+|j|} - H_{dp,-|j|})/2$. (c) Schematics of the DW magnetization configuration as a function of the IP field H_x. The blue arrows indicate the direction of the IP field. (d) Spin Hall efficiency χ as a function of H_x for up-down (blue) and down-up (red) DWs on Pt/TmIG/NGG. Solid lines are fit using the 1D DW model (see Sec. VI). (e) Effective spin Hall angles for TmIG on various substrates.

Figure 3(d) summarizes χ as a function of H_x. The normalized spin Hall efficiency $\chi/\chi_0 \equiv \cos\psi$ directly reveals how the DW magnetization is reoriented by the application of the IP field. For both up-down and down-up polarities, the wall shows a nonzero and opposite Néel character, indicating a right-handed wall chirality and a nonzero iDMI. The curves can be interpreted as the hard-axis hysteresis loop of the DW itself, as described in Ref. [31]. Fitting the data using a one-dimensional (1D) DW model [solid lines in Fig. 3(d); see Sec. VI], we extracted $\mu_0 H_D = 5.1$ mT from the horizontal intercept and $\mu_0 H_{K,DW} = 24.9$ mT from the width of the central part of the piecewise function. The above process was repeated on all the TmIG samples on different substrates, yielding a hysteresis loop for each.

From the magnitude of the depinning curves we can extract the effective spin Hall angle θ_{eff} according to the equation $\chi_0 \equiv \frac{\pi}{2} \frac{\hbar \theta_{eff}}{2\mu_0 e M_s t}$ [Fig. 3(e)]. θ_{eff} depends on the spin-mixing conductance [54] of the Pt/TmIG interface; in other words, it depends on the interface spin transparency. The spin-polarized current from the Pt layer which passes into the TmIG experiences spin backflow [55] and scattering [56,57],

which reduces the transmitted spin current. θ_{eff} is therefore smaller than the reported intrinsic spin Hall angle of Pt, which is 8% [58]. The data points show $\theta_{eff} \sim 5\%$ with little variation among all the samples, implying that the spin transparency of the Pt/TmIG interface is constant across the sample series.

A. Comparison of DW width obtained from DW depinning and SMR measurements

From the $H_{K,DW}$ values obtained in DW depinning measurements, we can extract a DW width Δ^{dp} from $H_{K,DW} = \frac{t \ln(2) M_s}{\pi \Delta}$ [31,59] (see Sec. VI); from the SMR measurement we can calculate Δ in a different manner: $\Delta^{SMR} = \sqrt{\frac{A}{K_{u,eff}}}$ [59], with A, the exchange stiffness, taken to be that of YIG, 3.7 ± 0.4 pJ/m [48]. Figure 4(a) shows a comparison of the two sets of measurements of DW widths, with the depinning (SMR) values plotted as the vertical (horizontal) coordinate. The blue line shows the expectation of equality. We speculate that the deviation of Δ^{dp} from Δ^{SMR} is mainly due to the limitation of the number of data points in a set of depinning
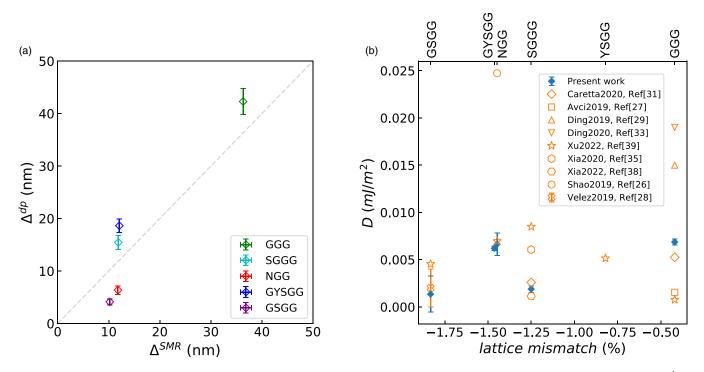
FIG. 4. DW width and DMI for TmIG on various substrates. (a) DW width Δ from DW depinning and SMR measurements. Δ^{dp} is plotted as a function of Δ^{SMR}. Error bars are the propagated error of $H_{K,DW}$. The expectation is $\Delta^{\mathrm{dp}} = \Delta^{\mathrm{SMR}}$, shown as the gray dashed line. (b) Substrate dependence of iDMI in TmIG. Solid symbols show the iDMI strength D extracted using H_D in the depinning measurements and Δ from SMR, plotted as a function of the substrate lattice parameter. Error bars are the propagated error of H_D. Data from other references are shown as open symbols.

measurements [Fig. 3(d)] since $H_{K,\mathrm{DW}}$ is extracted from the width of the inclined region. $H_{K,\mathrm{SMR}}$, on the other hand, is extracted from the saturation of R_H in Fig. 2(b), which has more data points for fitting and thus smaller uncertainty. We therefore use the SMR data for the DW width in the following iDMI calculations.

B. Substrate dependence of iDMI in TmIG

On the depinning curves of the down/up wall for all the samples, we find the same sign for the horizontal intercept, indicating the same right-handed iDMI chirality for TmIG on all the substrates. Following previous work on the Pt/garnet/substrate [27,28,30,31], a possible explanation is that the Pt/TmIG interface yields right-handed chirality and the TmIG/substrate interface yields right-handed chirality or left-handed chirality but with smaller magnitude. The iDMI strength D was extracted by $H_D = \frac{D}{\mu_0 M_s \Delta}$ [9] using Δ^{SMR} and is summarized by the filled diamonds in Fig. 4(b). TmIG on GGG, NGG, and GYSGG samples gives the largest iDMI. D does not show a clear trend with the lattice strain of TmIG. For example, SGGG has almost the same lattice parameter as GYSGG and NGG, but the iDMI is smaller by a factor of 3.4. This conclusion may be compared to a recent work which showed that DMI changed nonmonotonically with strain, peaking for TmIG/SGGG [39]. The data for D show good agreement with the previously reported magnitude of iDMI for Pt(4)/TmIG(6)/GGG and Pt(4)/TmIG(6)/SGGG [31]. Other TmIG references yield iDMI of the same order of magnitude as shown in Fig. 4(b), where data are scaled by the nominal thickness of TmIG.

V. CONCLUSION

By DW depinning measurements, we measured the iDMI and DW width in Pt/TmIG thin films on various garnet substrates (GGG, SGGG, NGG, GYSGG, and GSGG). Films of TmIG on all of the substrates have clearly measurable iDMI (except for that on GSGG), all of which show right-handed chirality. We demonstrated that the magnitude of iDMI is sensitive to the substrate but D does not simply scale with lattice mismatch. On the other hand, both transport and DW measurements show that by varying the lattice mismatch, we can effectively tune the strain-induced anisotropy of the film and hence the DW width. In racetrack memory devices where bits are encoded with homochiral skyrmions or DWs, a stronger D and/or a wider Δ can lead to a faster propagation speed of these magnetic structures at a fixed current injection [8,9,60–64]. Our results therefore expand the current knowledge of potential garnet-based spintronic devices with desirable properties such as low damping and Joule heating compared to metallic devices. This study clarifies the strain/substrate dependence of iDMI, which is relevant for further understanding the iDMI mechanisms in garnet thin-film systems.

VI. METHODS

A. Growth, patterning, and characterization

TmIG films were deposited using PLD on single-crystal GGG, SGGG, NGG, GYSGG, and GSGG substrates at 200 mTorr pressure and 720 °C. The PLD used a 248 nm wavelength KrF excimer laser with a 10 Hz repetition rate

and laser fluence of 1.5 J/cm. The target was a commercially available TmIG target with a 99.99% elemental purity. The target-substrate distance was fixed at 6 cm. HRXRD measurements were carried out in a Bruker D8 Discover. Film thickness was determined by HRXRR. Pt metallic overlayers were grown using dc magnetron sputtering with an Ar sputter gas pressure of 3 mTorr and a background base pressure of 1×10^{-7} Torr. Deposition rates were calibrated using x-ray reflectivity. After deposition, TmIG films were patterned to make Hall crosses and DW track devices. Maskless lithography was done using a Heidelberg DirectWrite-MLA-150-OptAF. The patterned film was then ion milled with Ar plasma, leaving behind only regions protected by the resist.

B. SMR and wide-field MOKE measurements

SMR measurements were performed on 100×40 μm^2 devices. Hall effect measurements reported in Fig. 2 were performed by injecting an ac voltage of $V_{rms} = 5$ V with frequency $\omega/2\pi = 9.973$ kHz, giving rise to a current of amplitude $I_{rms} = 0.5$ mA, using a standard lock-in amplifier. A typical device resistance was $R_{device} \approx 500\ \Omega$, to which a resistor of $10\,\mathrm{k}\Omega$ was connected in series. The IP magnetic field is swept over a range of ~ 0.7 T. The measured ac Hall voltage at each applied field was averaged over several acquisitions and was converted to a Hall resistance using $R_H = (V/I)$.

Spin Hall torque magnetometry was performed on 50×10 μm^2 tracks. Polar MOKE measurements were performed on a custom-built, wide-field Kerr microscope with independent OP and IP magnetic field control. Kohler illumination was used with a $10\times$ objective. The light source was a 456.6 nm wavelength LED.

Adopting a 1D DW model, the DW surface energy σ satisfies [9,62]

$$
\begin{aligned}
\frac{\sigma}{2\Delta\mu_0 M_S} = {} & \frac{1}{2}H_{K,\mathrm{DW}}\cos^2\psi + Q\frac{\pi}{2}H_D\cos\psi - \frac{\pi}{2}H_y\sin\psi \\
& - \frac{\pi}{2}H_x\cos\psi + \frac{\sqrt{AK_{u,\mathrm{eff}}}}{\Delta\mu_0 M_S} + \text{Zeeman term},
\end{aligned}
\tag{3}
$$

where the last two terms are constant. H_D is the DMI effective field, $H_{K,DW}$ is the DW shape anisotropy field, $Q = 1$ for the up-down wall, and $Q = -1$ for the down-up wall. Minimizing σ gives the stable state of ψ. In our scenario of $H_y = 0$, for the up-down wall we have a stable state:

$$
\cos\psi = \begin{cases}
+1 & (H_x - H_D) > \frac{2}{\pi}H_{K,\mathrm{DW}}, \\
\frac{\pi}{2}\frac{H_x - H_D}{H_{K,\mathrm{DW}}} & -\frac{2}{\pi}H_{K,\mathrm{DW}} < (H_x - H_D) < \frac{2}{\pi}H_{K,\mathrm{DW}}, \\
-1 & (H_x - H_D) < -\frac{2}{\pi}H_{K,\mathrm{DW}}.
\end{cases}
\tag{4}
$$

When passing a current through the Pt overlayer, the spin-orbit torque acts on the DW as an OP effective field, $H_{\mathrm{eff}} \equiv \chi j \equiv \chi_0 \cos\psi\, j$, where $\chi_0 \equiv \frac{\pi}{2}\frac{\hbar\theta_{\mathrm{eff}}}{2\mu_0 e M_s t}$. θ_{eff} is the effective spin Hall angle, and t is the magnetic film thickness. Thus, by measuring the current effective field we can probe the DW orientation ψ.

We measured H_{eff} by directly observing current-assisted DW depinning events under wide-field MOKE [Fig. 3(a)]. A small constant dc current is injected through the DW track, and a static H_z is applied and ramped until the wall depins and moves to the left, which happens at $H_z = H_{\mathrm{dp}}$. The role of the dc current is to generate an H_{eff} along the z direction to assist the applied H_z with depinning the DW. By measuring δH_{dp} we obtain H_{eff} and therefore obtain $\cos\psi$ [Fig. 3(b)]. By performing the measurement under various H_x and fitting it to Eq. (4) we extracted H_D and $H_{K,\mathrm{DW}}$ [Fig. 3(d)].

The expressions for these two effective fields read [9,31,59]

$$
H_D = \frac{D}{\mu_0 M_s \Delta}
\tag{5}
$$

$$
H_{K,\mathrm{DW}} = \frac{t\ln(2)M_s}{\pi\Delta}
\tag{6}
$$

Data are available from the authors on reasonable request.

[1] I. Dzyaloshinsky, J. Phys. Chem. Solids **4**, 241 (1958).

[2] T. Moriya, Phys. Rev. **120**, 91 (1960).

[3] A. Fert, V. Cros, and J. Sampaio, Nat. Nanotechnol. **8**, 152 (2013).

[4] J. Sampaio, V. Cros, S. Rohart, A. Thiaville, and A. Fert, Nat. Nanotechnol. **8**, 839 (2013).

[5] W. Jiang, P. Upadhyaya, W. Zhang, G. Yu, M. B. Jungfleisch, F. Y. Fradin, J. E. Pearson, Y. Tserkovnyak, K. L. Wang, O. Heinonen, S. G. Te Velthuis, and A. Hoffmann, Science **349**, 283 (2015).

[6] S. Woo, K. Litzius, B. Krüger, M. Y. Im, L. Caretta, K. Richter, M. Mann, A. Krone, R. M. Reeve, M. Weigand, P. Agrawal, I. Lemesh, M. A. Mawass, P. Fischer, M. Kläui, and G. S. D. Beach, Nat. Mater. **15**, 501 (2016).

[7] O. Boulle *et al.*, Nat. Nanotechnol. **11**, 449 (2016).

[8] L. Caretta, M. Mann, F. Büttner, K. Ueda, B. Pfau, C. M. Günther, P. Hessing, A. Churikova, C. Klose, M. Schneider, D. Engel, C. Marcus, D. C. Bono, K. Bagschik, S. Eisebitt, and G. S. D. Beach, Nat. Nanotechnol. **13**, 1154 (2018).

[9] A. Thiaville, S. Rohart, É. Jué, V. Cros, and A. Fert, Europhys. Lett. **100**, 57002 (2012).

[10] S. Emori, U. Bauer, S. M. Ahn, E. Martinez, and G. S. D. Beach, Nat. Mater. **12**, 611 (2013).

[11] K. S. Ryu, L. Thomas, S. H. Yang, and S. S. P. Parkin, Nat. Nanotechnol. **8**, 527 (2013).

[12] S. S. Parkin, M. Hayashi, and L. Thomas, Science **320**, 190 (2008).

[13] S. Parkin and S.-H. Yang, Nat. Nanotechnol. **10**, 195 (2015).

[14] S. Mühlbauer, B. Binz, F. Jonietz, C. Pfleiderer, A. Rosch, A. Neubauer, R. Georgii, and P. Böni, Science **323**, 915 (2009).

[15] X. Z. Yu, Y. Onose, N. Kanazawa, J. H. Park, J. H. Han, Y. Matsui, N. Nagaosa, and Y. Tokura, Nature (London) **465**, 901 (2010).

[16] X. Z. Yu, N. Kanazawa, Y. Onose, K. Kimoto, W. Z. Zhang, S. Ishiwata, Y. Matsui, and Y. Tokura, Nat. Mater. **10**, 106 (2011).

[17] S. Seki, X. Z. Yu, S. Ishiwata, and Y. Tokura, Science **336**, 198 (2012).

[18] D.-H. Kim, M. Haruta, H.-W. Ko, G. Go, H.-J. Park, T. Nishimura, D.-Y. Kim, T. Okuno, Y. Hirata, Y. Futakawa, H. Yoshikawa, W. Ham, S. Kim, H. Kurata, A. Tsukamoto, Y. Shiota, T. Moriyama, S.-B. Choe, K.-J. Lee, and T. Ono, Nat. Mater. **18**, 685 (2019).

[19] M. Bode, M. Heide, K. Von Bergmann, P. Ferriani, S. Heinze, G. Bihlmayer, A. Kubetzka, O. Pietzsch, S. Blügel, and R. Wiesendanger, Nature (London) **447**, 190 (2007).

[20] L. Liu, C. F. Pai, Y. Li, H. W. Tseng, D. C. Ralph, and R. A. Buhrman, Science **336**, 555 (2012).

[21] S. Woo, M. Mann, A. J. Tan, L. Caretta, and G. S. Beach, Appl. Phys. Lett. **105**, 212404 (2014).

[22] A. Fert and P. M. Levy, Phys. Rev. Lett. **44**, 1538 (1980).

[23] M. Bibes and A. Barthélémy, IEEE Trans. Electron Devices **54**, 1003 (2007).

[24] A. Bhattacharya and S. J. May, Annu. Rev. Mater. Res. **44**, 65 (2014).

[25] A. V. Chumak, V. I. Vasyuchka, A. A. Serga, and B. Hillebrands, Nat. Phys. **11**, 453 (2015).

[26] Q. Shao, Y. Liu, G. Yu, S. K. Kim, X. Che, C. Tang, Q. L. He, Y. Tserkovnyak, J. Shi, and K. L. Wang, Nat. Electron. **2**, 182 (2019).

[27] C. O. Avci, E. Rosenberg, L. Caretta, F. Büttner, M. Mann, C. Marcus, D. C. Bono, C. A. Ross, and G. S. D. Beach, Nat. Nanotechnol. **14**, 561 (2019).

[28] S. Vélez, J. Schaab, M. S. Wörnle, M. Müller, E. Gradauskaite, P. Welter, C. Gutgsell, C. Nistor, C. L. Degen, M. Trassin, M. Fiebig, and P. Gambardella, Nat. Commun. **10**, 4750 (2019).

[29] S. Ding, A. Ross, R. Lebrun, S. Becker, K. Lee, I. Boventer, S. Das, Y. Kurokawa, S. Gupta, J. Yang, G. Jakob, and M. Kläui, Phys. Rev. B **100**, 100406(R) (2019).

[30] S. Vélez, S. Ruiz-Gómez, J. Schaab, E. Gradauskaite, M. S. Wörnle, P. Welter, B. J. Jacot, C. L. Degen, M. Trassin, M. Fiebig, and P. Gambardella, Nat. Nanotechnol. **17**, 834 (2022).

[31] L. Caretta, E. Rosenberg, F. Büttner, T. Fakhrul, P. Gargiani, M. Valvidares, Z. Chen, P. Reddy, D. A. Muller, C. A. Ross, and G. S. D. Beach, Nat. Commun. **11**, 1090 (2020).

[32] F. Trier, P. Noël, J. V. Kim, J. P. Attané, L. Vila, and M. Bibes, Nat. Rev. Mater. **7**, 258 (2022).

[33] S. Ding, L. Baldrati, A. Ross, Z. Ren, R. Wu, S. Becker, J. Yang, G. Jakob, A. Brataas, and M. Kläui, Phys. Rev. B **102**, 054425 (2020).

[34] H. Wang, J. Chen, T. Liu, J. Zhang, K. Baumgaertl, C. Guo, Y. Li, C. Liu, P. Che, S. Tu, S. Liu, P. Gao, X. Han, D. Yu, M. Wu, D. Grundler, and H. Yu, Phys. Rev. Lett. **124**, 027203 (2020).

[35] S. Xia, S. Zhang, Z. Luan, L. Zhou, J. Liang, G. Liu, B. Yang, H. Yang, R. Liu, and D. Wu, Appl. Phys. Lett. **116**, 052404 (2020).

[36] A. J. Lee, A. S. Ahmed, J. Flores, S. Guo, B. Wang, N. Bagués, D. W. McComb, and F. Yang, Phys. Rev. Lett. **124**, 107201 (2020).

[37] A. J. Lee, S. Guo, J. Flores, B. Wang, N. Bagués, D. W. McComb, and F. Yang, Nano Lett. **20**, 4667 (2020).

[38] S. Y. Xia, T. Feng, B. Yang, G. Liu, Y. Z. Tian, P. Wang, X. G. Wan, B. G. Wang, and D. Wu, Phys. Rev. B **105**, 184417 (2022).

[39] Z. Xu, Q. Liu, Y. Ji, X. Li, J. Li, J. Wang, and L. Chen, ACS Appl. Mater. Interfaces **14**, 16791 (2022).

[40] R. C. O'Handley, *Modern Magnetic Materials: Principles and Applications* (Wiley, New York, 1999), pp. 107–112.

[41] D. H. Kim, N. M. Aimon, L. Bi, J. M. Florez, G. F. Dionne, and C. A. Ross, J. Phys.: Condens. Matter **25**, 026002 (2013).

[42] A. Quindeau, C. O. Avci, W. Liu, C. Sun, M. Mann, A. S. Tang, M. C. Onbasli, D. Bono, P. M. Voyles, Y. Xu, J. Robinson, G. S. D. Beach, and C. A. Ross, Adv. Electron. Mater. **3**, 1600376 (2017).

[43] E. R. Rosenberg, L. Beran, C. O. Avci, C. Zeledon, B. Song, C. Gonzalez-Fuentes, J. Mendil, P. Gambardella, M. Veis, C. Garcia, G. S. D. Beach, and C. A. Ross, Phys. Rev. Mater. **2**, 094405 (2018).

[44] E. R. Rosenberg, K. Litzius, J. M. Shaw, G. A. Riley, G. S. Beach, H. T. Nembach, and C. A. Ross, Adv. Electron. Mater. **7**, 2100452 (2021).

[45] C. O. Avci, A. Quindeau, C. F. Pai, M. Mann, L. Caretta, A. S. Tang, M. C. Onbasli, C. A. Ross, and G. S. D. Beach, Nat. Mater. **16**, 309 (2017).

[46] K.-H. Hellwege and A. M. Hellwege, *Landolt-Börnstein: Group III Crystal and Solid State Physics* (Springer, Berlin, 1978), Vol. 12a.

[47] https://www.mtixtl.com, MTI Corporation (2023).

[48] S. Klingler, A. Chumak, T. Mewes, B. Khodadadi, C. Mewes, C. Dubs, O. Surzhenko, B. Hillebrands, and A. Conca, J. Phys. D **48**, 015001 (2015).

[49] C. Hahn, G. de Loubens, O. Klein, M. Viret, V. V. Naletov, and J. Ben Youssef, Phys. Rev. B **87**, 174417 (2013).

[50] N. Vlietstra, J. Shan, V. Castel, B. J. van Wees, and J. B. Youssef, Phys. Rev. B **87**, 184421 (2013).

[51] S. Meyer, R. Schlitz, S. Geprägs, M. Opel, H. Huebl, R. Gross, and S. T. Goennenwein, Appl. Phys. Lett. **106**, 132402 (2015).

[52] T. B. Bateman, J. Appl. Phys. **37**, 2194 (1966).

[53] S. Emori, E. Martinez, K.-J. Lee, H.-W. Lee, U. Bauer, S.-M. Ahn, P. Agrawal, D. C. Bono, and G. S. D. Beach, Phys. Rev. B **90**, 184427 (2014).

[54] C.-F. Pai, Y. Ou, L. H. Vilela-Leão, D. C. Ralph, and R. A. Buhrman, Phys. Rev. B **92**, 064426 (2015).

[55] P. M. Haney, H.-W. Lee, K.-J. Lee, A. Manchon, and M. D. Stiles, Phys. Rev. B **87**, 174411 (2013).

[56] J.-C. Rojas-Sánchez, N. Reyren, P. Laczkowski, W. Savero, J.-P. Attané, C. Deranlot, M. Jamet, J.-M. George, L. Vila, and H. Jaffrès, Phys. Rev. Lett. **112**, 106602 (2014).

[57] Y. Liu, Z. Yuan, R. J. H. Wesselink, A. A. Starikov, and P. J. Kelly, Phys. Rev. Lett. **113**, 207202 (2014).

[58] L. Liu, T. Moriyama, D. C. Ralph, and R. A. Buhrman, Phys. Rev. Lett. **106**, 036601 (2011).

[59] S. V. Tarasenko, A. Stankiewicz, V. V. Tarasenko, and J. Ferré, J. Magn. Magn. Mater. **189**, 19 (1998).

[60] I. M. Miron, T. Moore, H. Szambolics, L. D. Buda-Prejbeanu, S. Auffret, B. Rodmacq, S. Pizzini, J. Vogel, M. Bonfim, A. Schuhl, and G. Gaudin, Nat. Mater. **10**, 419 (2011).

[61] E. Martinez, S. Emori, and G. S. D. Beach, Appl. Phys. Lett. **103**, 072406 (2013).

[62] E. Martinez, S. Emori, N. Perez, L. Torres, and G. S. D. Beach, J. Appl. Phys. **115**, 213909 (2014).

[63] S. H. Yang, K. S. Ryu, and S. S. P. Parkin, Nat. Nanotechnol. **10**, 221 (2015).

[64] O. Alejos, V. Raposo, L. Sanchez-Tejerina, R. Tomasello, G. Finocchio, and E. Martinez, J. Appl. Phys. **123**, 013901 (2018).